

1 Earthquake-induced landslides monitoring and survey by means of 2 InSAR

3 Tayeb SMAIL¹, Mohamed ABED¹, Ahmed MEBARKI^{2,3}, Milan Lazecky^{4,5}

4 ¹Department of Civil Engineering, Saad Dahlab University, Blida City, Algeria

5 ²Univ Gustave Eiffel, Univ Paris Est Creteil, CNRS, UMR 8208, MSME, 5 Bd Descartes, F-77454 Marne-la-Vallée, France

6 ³Nanjing Tech University, 5 New Mofan Rd, Gulou, Nanjing, Jiangsu, Chine - Permanent Guest Professor within “High-
7 Level Foreign Talents Programme” grant

8 ⁴IT4Innovations, VSB-TU Ostrava, 17, Listopadu 15, 70833 Ostrava-Poruba, Czech Republic

9 ⁵School of Earth and Environment, University of Leeds, Leeds LS2 9JT, UK

10 *Correspondence to:* SMAIL Tayeb (st_gc@hotmail.fr)

11 **Abstract.** This study uses interferometric SAR techniques to identify and track earthquake-induced landslides as well as lands
12 prone to landslides, by detecting deformations in areas struck by earthquakes. The pilot study area investigates the Mila region
13 in Algeria, which suffered significant landslides and structural damages (earthquake: Mw5, 2020-08-07). DInSAR analysis
14 shows normal interferograms with small fringes. The Coherence Change Detection (CCD) and DInSAR analysis were able to
15 identify many landslides and ground deformations confirmed also by Sentinel-2 optical images and field inspection. The most
16 important displacement (2.5 m), located in Kherba neighborhood, caused severe damages to dwellings. It is worth notice that
17 CCD and DInSAR are very useful since they were also able to identify ground cracks surrounding a large zone (3.94 Km²
18 area) in Grarem City whereas the Sentinel-2 optical images could not detect them. Although, displacement time-series analysis
19 of 224 interferograms (04-2015 to 09-2020) performed using LiCSBAS did not detect any pre-event geotechnical precursors,
20 the post-event analysis shows a 110 mm/y subsidence velocity in the back-hillside of Kherba.

21 1 Introduction

22 Although it is still challenging to predict exactly where and when natural hazards (earthquakes, landslides, floods, etc.) might
23 occur, the capacity to monitor and survey the zones prone to important landslides as well as the capacity to identify and locate
24 those impacted by earthquakes are key issues in risks mitigation, reduction, preparedness and adaptation. Actually, since
25 earthquakes and landslides might occur in many places worldwide, they might cause a huge number of victims, important
26 socio-economic, assets damages and losses. Their impact can be significantly reduced thanks to satellite imaging which allows
27 prediction and early alerts of some landslide cases (Del and Idrogeologico, 2012; Jacquemart and Tiampo, 2021; Moretto et
28 al., 2021).

29 It is then worth detecting or predicting critical ground changes at specific places, either after a geotechnical hazard occurs
30 due to landslides and earthquakes mainly, or before it is suddenly triggered (Bakon et al., 2014; Galve et al., 2015). Such
31 challenges can be tackled by regular image processing oriented landslides areas monitoring, in the aftermath of earthquakes,
32 using SAR interferometric methods and optical images, for instance. Actually, since SAR (Synthetic Aperture Radar) is an
33 active sensor system that uses microwave signals to collect data backscattered from the earth’s surface, the use of satellite
34 imaging systems like Interferometric SAR methods appears as a cost-effective way for measuring millimeter-level
35 displacements of the earth surface (Herrera et al., 2009), at a regional scale and can be used as an early warning system for the
36 safety of structures and their surroundings (Galve et al., 2015; Roque et al., 2015).

37 The expected outcomes are based upon the processing of SAR data as it uses Differential InSAR (DInSAR), Coherence
38 Change Detection (CCD), and time series analysis (LiCSBAS software). LiCSBAS exploits the LiCSAR data that process
39 InSAR datasets automatically (Sentinel-1), taking advantage of high-resolution SAR sensing, in order to track ground changes
40 and landslides.

41 The SAR analyses aim to detect ground deformations through DInSAR and CCD investigations as they consider, for
42 illustrative purposes, a city in Algeria struck by an earthquake (August 7, 2020: Algeria, Mila): the ground deformations and
43 displacements, in Kherba City and Grarem City (northeastern part of Mila downtown, 2 km) are investigated. The affected
44 areas span over 3.94 km² for Grarem and 2.1 km² for the Kherba landslides. Furthermore, a time-series analysis of LiCSAR
45 data performed out by LiCSBAS software, investigates the possible existence of precursors in geotechnical conditions.

46 **2 Land and ground movements monitoring and surveying in the aftermath of an earthquake**

47 **2.1 Satellite images and methods - Case study**

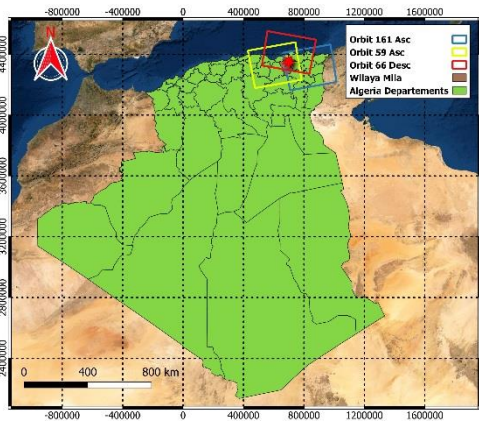
48 The present research study is multifold. It aims to use InSAR image processing for various purposes, in the case of landslides
49 and earthquakes:

- 50 - Use the InSAR in the aftermath of an earthquake in order to identify the geotechnical displacements or deformations,
51 their extent, and locations. The Differential radar interferometry and the Coherence Changes Detection are the most
52 adapted methods for ground and soil surfaces changes detection (Jung and Yun, 2020; Meng et al., 2020; Pawluszek-
53 Filipiak and Borkowski, 2020; Tampuu et al., 2020; Tzouvaras et al., 2020). A city, Mila, in Northern Algeria, is
54 considered as the pilot study. It has been struck by an earthquake in August 2020. The landslides and surface cracks
55 have been affected significantly, during the earthquake events series, two distinct zones being distant by almost 15 km
56 from each other (Kherba and Grarem).
- 57 - Use time-series analysis to investigate the displacements and their velocities before and after the occurrence of the
58 main shock. For the city of Mila, the time series is performed out for a period extending from April 2015 up to October
59 2020, i.e. a long period before (*5 entire years*) the main shock in order to avoid a disturbance or bias that might be
60 related to seasonal effects such as rains and vegetation effects (Lazecq̃y et al., 2020a), and a short period (*4 months*)
61 ahead of the event date in order to investigate the historical development of the landslide.
- 62 - Compare and correlate the InSAR images processing results with the satellite optical images observations.

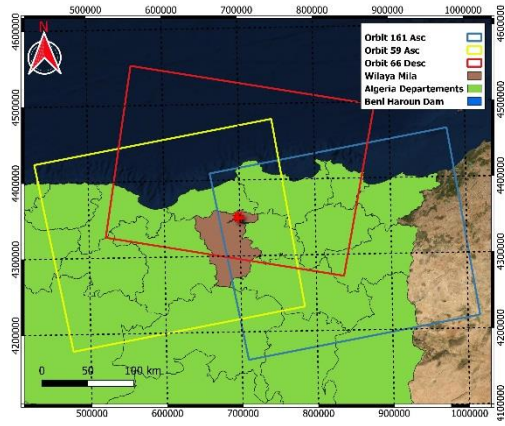
63 **2.2 Pilot zone, earthquakes and landslides - Observed disorders**

64 The case study area lies in Mila Province which is located in the northeast part of Algeria (Mediterranean zone), near the Dam
65 of Beni Haroun. The Mediterranean zone is seismically active because of the northward convergence (4-10 mm/yr) of the
66 African plate relative to the Eurasian plate along a complex plate boundary (Frizon de Lamotte et al., 2000; Mouloud and
67 Badreddine, 2017; Peláez Montilla et al., 2003; USGS). Throughout the last years, several landslide events have taken place in
68 the wider region of Mila (Merghadi et al., 2018). Merghadi et al.(2018) constructed a detailed landslide inventory map of the
69 study area. The seismic activities and landslides pose a persistent threat for built-up areas and facilities, such as roadways,
70 bridges and tunnels, which need continuous monitoring and survey.

71 After an earthquake (Mw 5, 2020-08-07, epicenter 36.550° N - 6.271° E, Depth=10 km, (USGS)) that struck this region,
72 important landslides were mostly observed in Mila City and its surroundings, see Figs. 1-3. Although, the earthquake was
73 moderate, Beni Haroun Dam and the two large bridges built on the RN 27 highway needs to be inspected and their possible
74 displacements monitored.



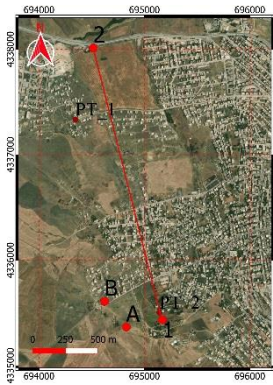
(a)



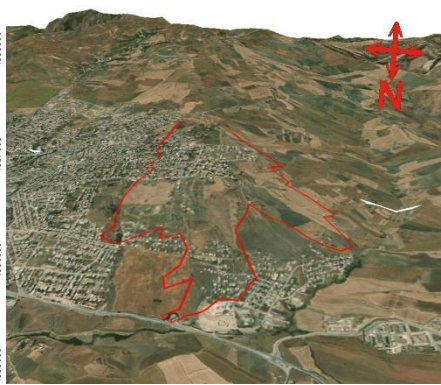
(b)

Figure 1. Mila location map (a), ascending and descending orbits footprints. Red stars indicate earthquake epicenter (QGIS, ESRI basemap).

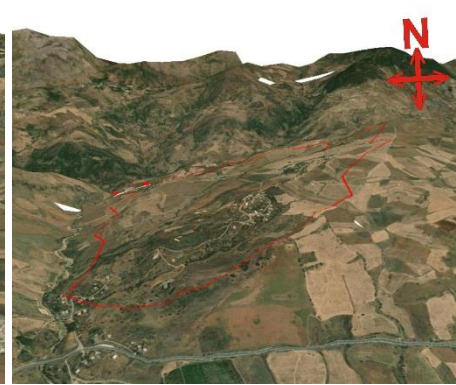
In the present, two areas are studied, i.e. Kherba and Grarem Cities. The altitude at the top point 1 (Fig. 2.a) in Kherba hill is 654 m and 411 m for the upper point (2), located at 2.14 km distance with 11.34% slope. The maximum ground horizontal offset reached 2.5 m and the vertical deformations exceed 1.8 m (Fig. 3.b) at the top of Kherba hill (point A Fig. 2.a). The slope failure boundary of Kherba City is mapped as shown in Fig. 2.b. The Grarem area of interest (AoI) is located east north of Mila in hilly ground with an average slope reaching 12.5%, see Fig. 2.c.



(a)



(b)



(c)

Figure 2. 3D view of AoIs, Kherba AoI and Grarem using QGIS with DEM SRTM 1sec and ESRI basemap, a & b are Kherba AoI, c is the Grarem case area, the red polygon is the boundary of change detected by InSAR.



(a)



(b)



(c)

Figure 3. Ground cracks due to landslides in Kherba, Mila, ~2.5m offset towards the North, a. Drone aerial photo from (LNHC), b. & c.- Lateral displacements (Photos: courtesy M. Yacoub A., University of Setif, Algeria).

2.3 Pilot zone - Data and images collection

The dataset used for this study is collected from European Space Agency (ESA), via the Copernicus Open Access portal, and from the Alaska Satellite Facility (ASF DAAC). The C-band Sentinel-1 A and B, launched in 2014 and 2016 respectively, provide regular datasets. The Sentinel-1 sensors have a wavelength of 5.546 cm (ESA), suitable for change detection and monitoring of large areas, and are right side-looking with an incidence angle ranging approximately from 20° to 46° (ESA,

96 2012). For the InSAR use, the Interferometric Wide (IW) swath Single Look Complex (SLC) data is selected and processed
 97 with the open-source software SNAP (Sentinel Applications Platform). It is worth using data from many orbits to monitor the
 98 AoIs due to different oriented directions, incidence angles of satellites, and the ground topography. The optical images of
 99 Sentinel-2 satellites are obtained from ESA, whereas downloading and processing data is done via QGIS, Semi-Automatic
 100 Classification Plugin (SCP) (Congedo, 2021).

101 For Mila region, the AoI is covered by 3 orbits, two are ascending (66, 59) and one is descending (161) (Fig. 1). Since the
 102 present study intends to detect the areas influenced by landslides, many pre-event and post-event data were used. Eighteen
 103 Sentinel-1 A and 17 Sentinel-1 B images (a total of 35) were downloaded to monitor Mila's area for the period from 1 July
 104 2020 to 26 October 2020. Table 1 summarizes the appropriate interferograms, i.e. those having small perpendicular baselines
 105 and short temporal baselines. Tables 1, 2, and 2bis present all the images, their labels as IFG-ID, Orbits, and dates of
 106 acquisition.

107 **Table 1.** Characteristics of Sentinel-1 InSAR pairs used for this study.

IFG-ID	Track	M Date	S Date	Bp [m]	Bt [days]
IFG-0		2020-07-22	2020-07-28	-9.99	6
IFG-1		2020-07-28	2020-08-03	40.90	6
IFG-2		2020-07-28	2020-08-03	40.62	6
IFG-3		2020-08-03	2020-08-09	-51.47	6
IFG-4		2020-08-03	2020-08-09	-50.76	6
IFG-5		2020-08-09	2020-08-15	-27.57	6
IFG-6		2020-08-09	2020-08-15	27.62	6
IFG-7	66 ASCENDING	2020-08-15	2020-08-21	-16.19	6
IFG-8		2020-08-21	2020-08-27	42.43	6
IFG-9		2020-08-27	2020-09-02	-28.59	6
IFG-10		2020-09-02	2020-09-08	29.26	6
IFG-11		2020-09-08	2020-09-14	17.95	6
IFG-12		2020-09-14	2020-09-20	-6.05	6
IFG-13		2020-09-20	2020-10-02	-4.64	12
IFG-14		2020-10-02	2020-10-14	18.13	12
IFG-15		2020-10-14	2020-10-26	-49.36	12
IFG-16		2020-07-27	2020-08-02	69.64	6
IFG-17		2020-08-02	2020-08-08	-75.10	6
IFG-18	59 ASCENDING	2020-08-08	2020-08-14	-8.86	6
IFG-19		2020-08-14	2020-08-20	175.97	6
IFG-20		2020-08-20	2020-08-26	-226.75	6
IFG-21		2020-07-22	2020-07-28	-169.19	6
IFG-22		2020-07-28	2020-08-09	30.39	12
IFG-23		2020-07-28	2020-08-03	99.88	6
IFG-24	161 DESCENDING	2020-08-03	2020-08-09	-70.12	6
IFG-25		2020-08-09	2020-08-15	2.14	6
IFG-26		2020-08-15	2020-08-21	121.22	6
IFG-27		2020-08-21	2020-08-27	-196.82	6

108 **Bt:** temporal baseline; **Bp:** perpendicular baseline.

109 The temporal baselines for all InSAR pairs are 6 days, except the last three pairs of the ascending orbit 66 that have 12 days.
 110 Furthermore, since a bad coherence map of the IFG-24 (Orbit 161), may lead to misinterpretation of results, prior acquisition
 111 data (before the 3rd of August) is selected to generate the co-event interferogram (IFG-22). Therefore the temporal baseline is
 112 12 days. The gray rows in Table 1 represent the co-event interferograms of the three orbits. The perpendicular baselines
 113 guarantee also a good quality of InSAR studies (Braun, 2019). As LiCSBAS time series analysis aims to investigate long
 114 period displacements and velocities over a large area: 34 interferograms from orbit 66 and 190 interferograms collected from
 115 the 161 ascending track (Table 2), are selected for the present study.

116 **Table 2.** LiCSAR frames, analyzing periods and the total number of IFGs used in this study.

Frame ID	Date		Period	IFGs
	Start	End		
161A_05343_090806	2015-4-26	2020-9-26	66 month	190
066D_05394_131311	2020-4-5	2020-9-26	6 months	34

117 **Table 2bis.** Sentinel-2 optical images collected for the study case.

Frame ID	Date	Duration days, to the main shock
Image 1	2020-07-30	-7 days
Image 2	2020-08-09	+ 2 days

118 3 Methodology description and results

119 Four aspects are investigated and compared in the present case study:

- 120 - The SAR Interferometric (InSAR) methodology, which is subdivided into three sub-groups:
- 121 - DInSAR for the phase changes (fringes),
- 122 - CDD for the coherence change detection,
- 123 - Time series analysis and LiCSAR data.
- 124 - The optical image processing.

125 Every image contains the description of its source, i.e. IFG-ID (Tables 1, 2, and 2bis) or the image's acquisitions dates.

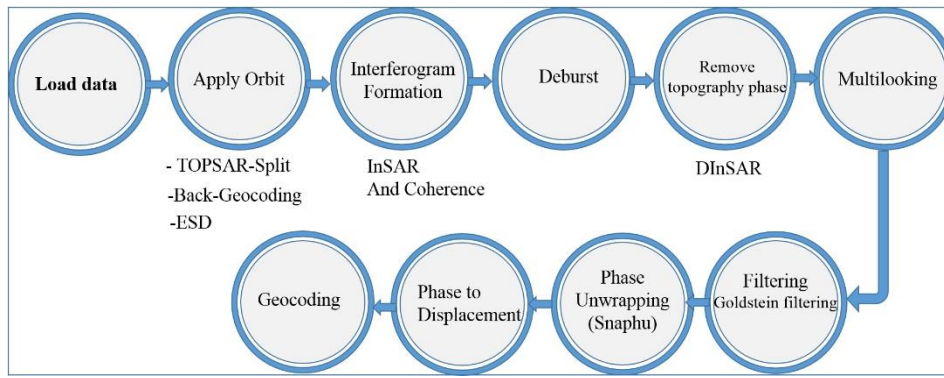
126 3.1 SAR Interferometric methodology

127 The Synthetic Aperture Radar (SAR) is an active microwave imaging system. It is independent of sunlight and penetrates
 128 clouds, unlike passive optical imaging systems. The interferometric SAR method uses the phase components of co-registered
 129 SAR images of the same pixel to estimate the topography and to measure the surface change in the target area (Kim, 2013).
 130 At least two constellation images are needed to generate an interferogram, which contains topographic, atmospheric effect,
 131 baseline error, and noise components (Goudarzi, 2010; Kim, 2013; Netzband et al., 2007):

$$132 \phi = \phi_{disp} + \phi_{flat} + \phi_{topo} + \phi_{atm} + \phi_{orbit} + \phi_{noise} \quad (1)$$

133 Where ϕ_{disp} is the line-of-sight (LOS) displacement, ϕ_{flat} the flat earth phase, ϕ_{topo} the topographic phase, ϕ_{atm} is an
 134 atmospheric phase, ϕ_{orbit} , the baseline phase and ϕ_{noise} is noise phase contribution (Kim, 2013).

135 The main steps of processing data using SNAP software (DInSAR and CCD) are depicted in Fig. 4. It's worth notice that
 136 for CCD processing, it is not necessary to follow the whole (DInSAR, Phase Unwrapping, and Phase to displacement).



137
138 **Figure 4.** Workflow chart for the DInSAR processing using (SNAP) software.

139 **3.1.1 Differential radar interferometry (DInSAR)**

140 Differential radar interferometry (DInSAR) exploits the phase difference to measure coherent changes or deformation between
141 two image acquisitions. It is often used for ground subsidence measurement (Canaslan Çomut et al., 2020; Galve et al., 2015).
142 One of DInSAR’s limitations is that the changes are not measurable in the case of non-coherent events (e.g., rapid landslide)
143 (Braun, 2019) such as the present study.

144 **3.1.2 Coherence Change Detection (CCD)**

145 The estimated coherence is considered as a quality indicator of an interferogram (Jacquemart and Tiampo, 2021). Actually, it
146 indicates that the phase and amplitude of the received signal express the degree of similarity between the images pair. The
147 pixel coherence γ of two SAR images is estimated on the basis of N neighboring pixels (Jia et al., 2019; Wang et al., 2018).

148
$$\gamma = \frac{\sum_{i=1}^N S_{1i} S_{2i}^*}{\sqrt{\sum_{i=1}^N |S_{1i}|^2 \sum_{i=1}^N |S_{2i}|^2}} \quad (2)$$

149 Where: S_{1i}, S_{2i} , are the complex signal values of the SAR image pair, N is the window of neighboring pixels, * is the complex
150 conjugate.

151 The coherence values range between 0 and 1 so that the map is represented as a gray color which 0 is white and 1 is black.

152 **3.1.3 Time series analysis and LiCSAR data**

153 The “Looking into Continents from Space with Synthetic Aperture Radar” (LiCSAR) system processes automatically Sentinel-
154 1 datasets for InSAR use, and generates wrapped, unwrapped interferograms and coherence maps (Lazecký et al., 2020b), with
155 a final product resolution of ~26.5 m (Lazecký et al., 2020a). For such purposes, the open-source LiCSBAS software, adopted
156 in the present study, is used for InSAR time series analysis based on LiCSAR data. It can generate maps of LOS displacement
157 velocity and deformation time series for all processed frames. Furthermore, it is easy to implement and does not request high-
158 performance computing facilities (Morishita, 2021).

159 In addition, the mechanism of landslides can be thoroughly studied through LiCSBAS analyses. They rely on the InSAR
160 time-series analysis package integrated with LiCSAR, (Lazecký et al., 2020b). Such time-series analyses are very useful in
161 identifying, for a given landslide or ground deformations and displacements, the prior patterns of ground movements versus
162 the time.

163 **3.2 Optical image processing**

164 The optical sensors are passive detection means that need sunlight and clear weather conditions to exploit the data. The
165 Sentinel-2 is a multi-spectral instrument (MSI) that measures reflected solar radiance in 13 bands with a spatial moderate-
166 resolution of 10 m in the red, green, blue, and near-infrared bands (Laneve et al., 2021).

167 The optical data collected from the ESA platform (Sentinel-2) is treated and plotted using QGIS software to generate true color
168 images (bands 2, 3, and 4 corresponding to RGB). The present study skips the image of 3rd, Aug 2020 due to bad weather
169 conditions, so that only the two images collected and mentioned in the table 2bis were used to validate the ground changes
170 detected by InSAR.

171 4 Application to the case study and results

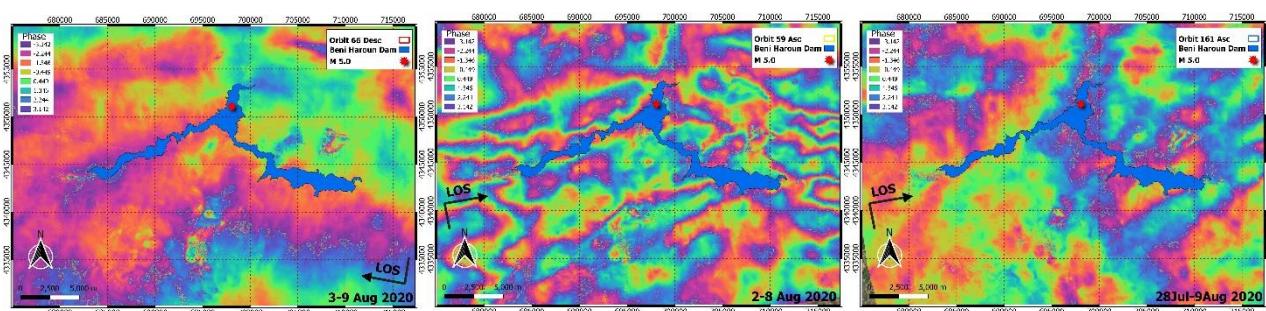
172 The case studies are located in two different sites and both areas of interest are located in Algeria. They have a hilly relief: the
173 first one is located northeast of Mila City (Grarem) and the second is at the west part of Mila City (Kherba). To monitor the
174 AoIs, several images are processed and used with different orbits directions (total of 35 ascending and descending acquisitions,
175 see Fig. 1), to catch deformation from different angles along the sensor's LOS. The InSAR technique is used in both areas, to
176 detect land deformation and landslides triggered by the earthquake.

177 The adopted methods are applied for Mila case study to:

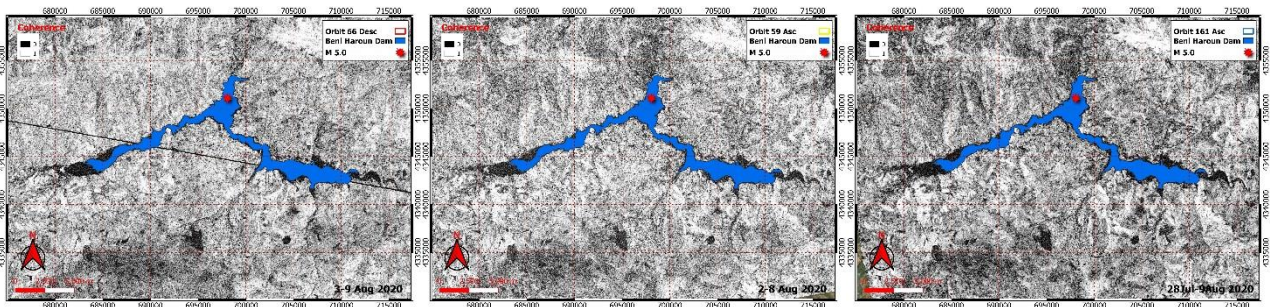
- 178 - detect and measure the co-event surface displacements and landslides, caused by the earthquake (CCD and DInSAR)
- 179 - monitor their dynamic evolution in the first weeks and months, at the post-event period (CCD and LiCSAR data).
- 180 - analyze their possible initiation ahead of the earthquake by months and years, at the pre-event period (Time-series
181 methods and LiCSAR data).
- 182 - corroborate the results by comparing several methods outputs, i.e. SAR (CCD, DInSAR, LiCSAR), aerial optical photo
183 (Sentinel-2), and field surveys.

184 The quality of the SAR image is consistent with the topography slopes and area roughness. Actually, the AoI has rough
185 topography, hills, and rivers (Fig. 2). Selecting either ascending or descending passes, relying on which will avoid some
186 limitation of InSAR is an extremely essential action to infer the deformation from various angles. Therefore, considering the
187 regional topography and geology of the AoI is necessary to process InSAR and results interpreting.

188 Differential InSAR (DInSAR) method is helpful to investigate co-seismic effects and detect ground changes. The produced
189 Interferograms and coherence images are projected to WGS84 reference, with a pixel size of 13.4 m. The unwrapped
190 interferograms present phase contribution of many noise resources (atmospheric), see Fig. 5. In general, strong earthquakes
191 cause large-scale fringes patterns around the epicenter which is not the case in the event under study (a moderate earthquake).
192 Processing DInSAR analysis may then lead to misinterpretation due to atmospheric contribution in differential phase
193 interferograms (Fig. 5). In the study case, no regional deformation due to the earthquake is observed and there is no need to
194 continue investigating the dam and the two bridges by simple DInSAR. However, to monitor the dam and bridges, it is highly
195 recommended to use PS-InSAR for regional and local ground deformation detection (Hooper et al., 2004; Rapant et al., 2020;
196 Sanabria et al., 2014).



197
198 **Figure 5.** Wrapped Interferograms from Sentinel-1 for IFG-3+IFG-4, IFG-17 and IFG-22, The red star is the epicenter location (USGS).

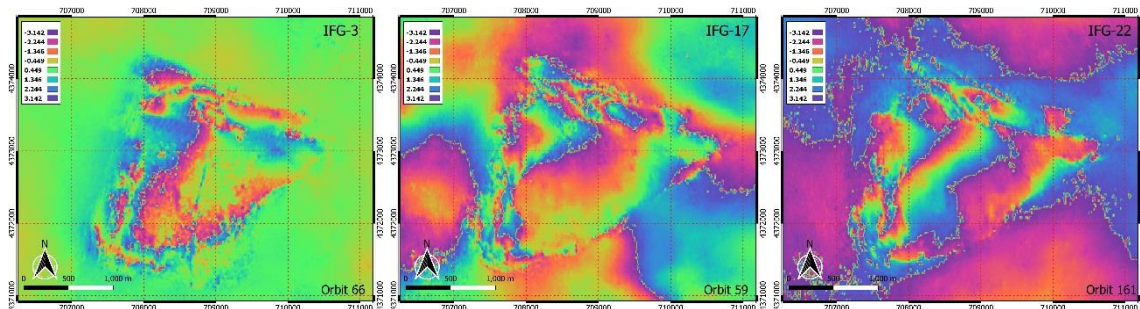


199
200 **Figure 6.** Mila Area, InSAR coherence maps for IFG-3+IFG-4, IFG-17 and IFG-22.

201 This moderate earthquake has triggered small deformation and landslides in Grarem, Kherba, and Azeba. The IFG-3 and
202 IFG-4 are merged in one image due to the AoIs (Kherba and Grarem), which are located in two different image acquisitions
203 of the descending orbit number 66.

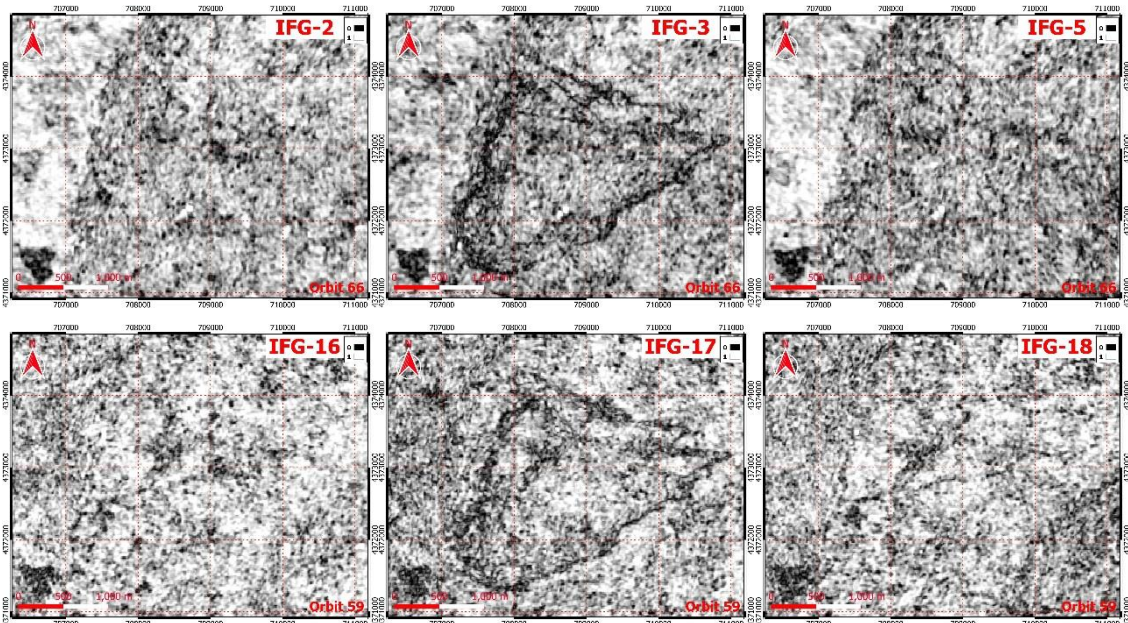
204 **4.1 Case of GRAREM**

205 The detection of deformation or changes between two InSAR images reveals a small change in the region of Grarem. This
206 change is observed as small fringes, each fringe corresponding to a displacement of a half-wavelength ($\lambda=5.546$ cm) in the
207 LOS direction (Fig. 7). Usually, coherent change does not appear in coherence images as dark region, but in the study case,
208 the outer borderline of the fringes region shows incoherence change which is clearly visible in coherence maps (Fig. 8).

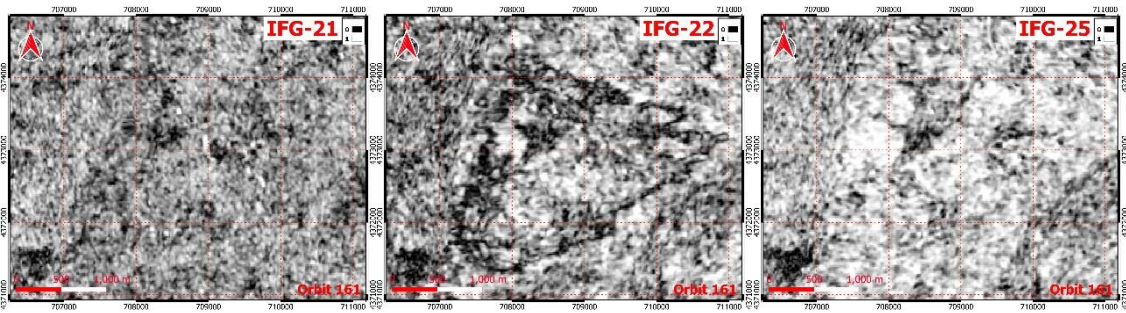


209
210 **Figure 7.** Detected fringes in Interferograms N° 3, 17, and 22, focused images on Grarem zone.

211 A time-series analysis needs then to be performed out to prove whether this contour was formed at the event occurrence
212 date (August 7, 2020). The coherence maps of the co-event period present a dark polygon that is related to incoherent change
213 or deformation. But inside the AoI, the results show some coherent changes which mean that this area has deformed as a block
214 up or down.

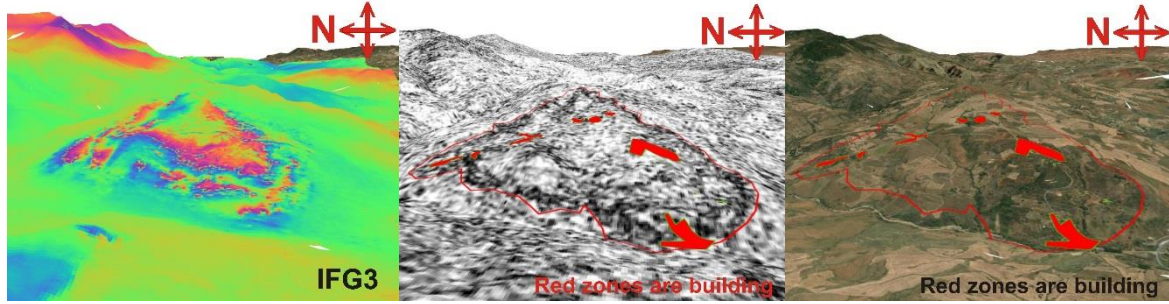


215
216



217
218 **Figure 8.** Coherence maps of Grarem AoI: the images represent pre-event (left), co-event (middle), and post-event (right) for orbits 66, 59,
219 and 161. *Nota: the co-event maps for the three orbits show the decay of coherence that is triggered by the earthquake.*

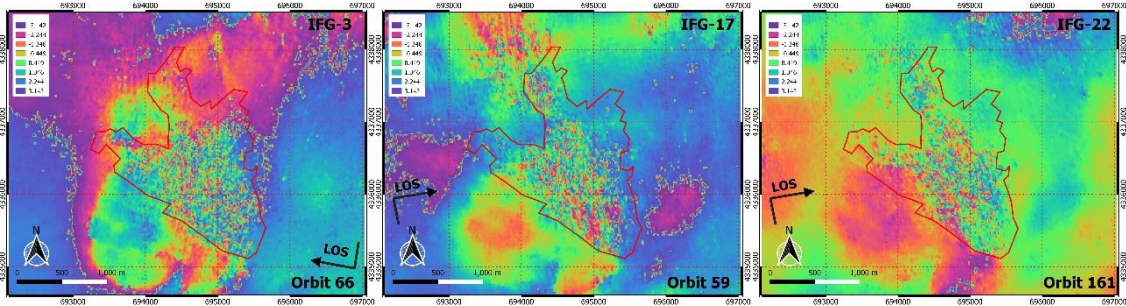
220 According to phase and coherence maps, the affected area is approximately 3.94 km², with an average runout distance of 2.6
221 km from top to downhill (Fig. 2.a distance from point 1 to point 2).



222
223 **Figure 9.** 3D view of Grarem Area, Images of IFG-3. Each fringe = wavelength/2 in LOS, and red zones represent existing building
224 compounds (QGIS, ESRI basemap).

225 4.2 Case of Kherba

226 DInSAR has abundantly demonstrated its reliability as a technique for monitoring slow movements (Cascini et al., 2013;
227 Wempen, 2020). In the present study, Kherba's landslides exceed the capabilities of DInSAR since this method cannot measure
228 the deformations due to incoherent change at the first event. Phase images of the Region of Interest (RoI) show a clear
229 decorrelation and consequently, the phase information is no longer convenient for analysis.



230
231 **Figure 10.** Kherba main event interferograms, biased pixels inside the red line correspond to incoherent changes.

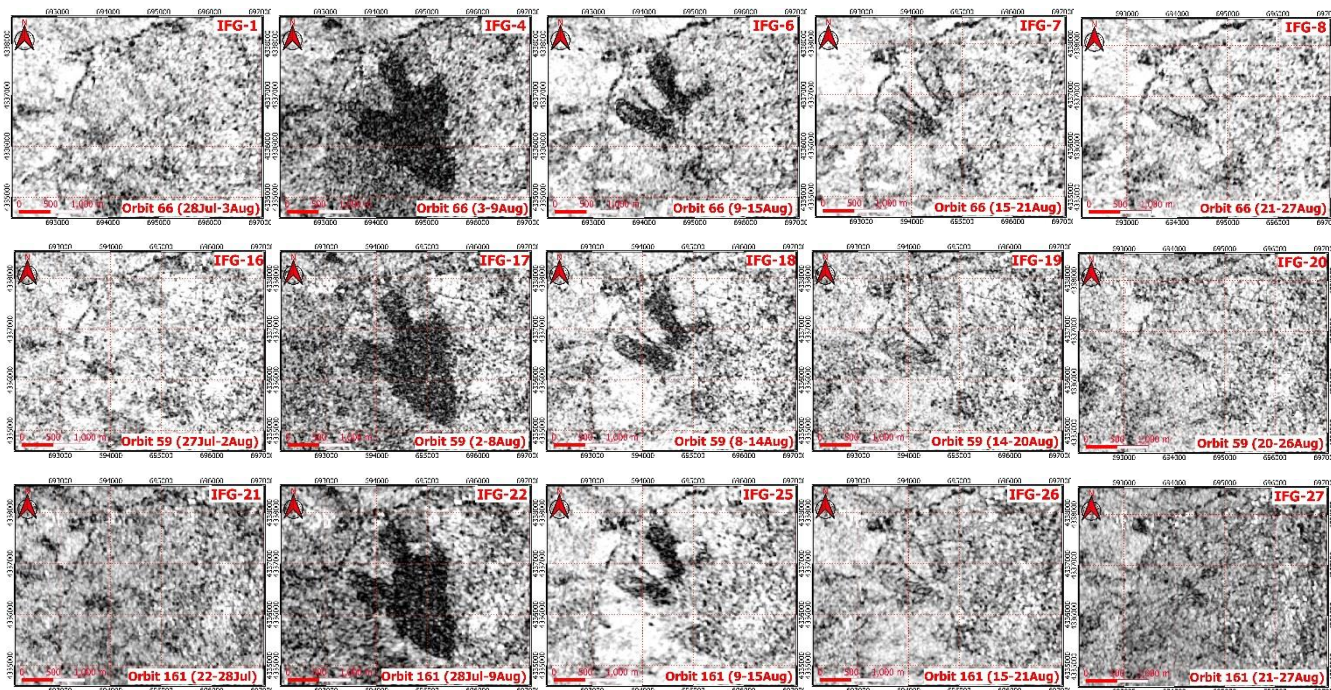
232 In such cases of incoherent changes in the scene, DInSAR is useless whereas the Coherence Change Detection (CCD) method
233 remains useful and suitable to monitor the event.

234 4.2.1 CCD Times series analyses

235 For the case study, the coherence maps (Figs. 11-13) show very low coherence in the Kherba area, indicating that some changes
236 have occurred. The CCD quantifies changes between two SAR images and is represented as a decay of coherence values (co-
237 event maps). Decreases in coherence values can be caused by a variety of factors such as geotechnical landslides as well as
238 water, vegetation. To distinguish between natural low coherence and induced surface changes, a second coherence map (pre-
239 event or post-event) is required to serve as a reference, which can be compared with the main co-event images. It is preferable

240 to mask out the rest of the non-changed area using a pre-event to co-event image ratio and filter values equal to or less than 1
 241 (see Fig. 13).

242



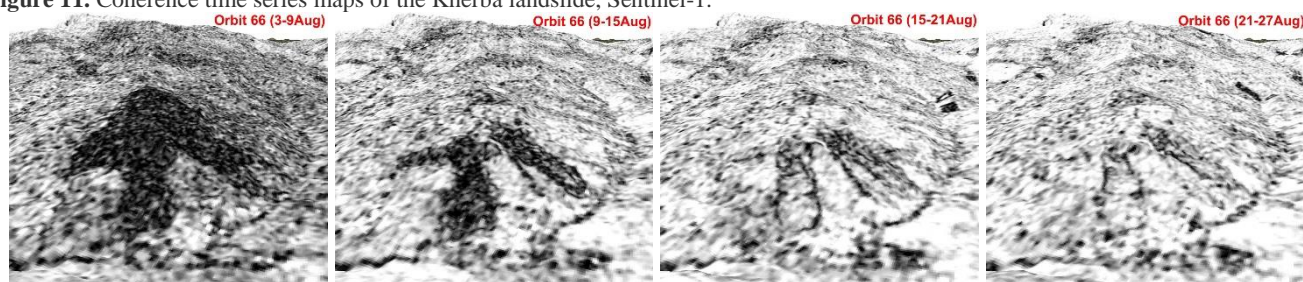
243

244

245

Figure 11. Coherence time series maps of the Kherba landslide, Sentinel-1.

246



247

248

Figure 12. 3D view of Kherba landslide, Sentinel-1 Coherence images of Orbit 66 with a 6-day temporal baseline, the dark areas are the landslide and deformations zones.

249

250

251

252

253

254

255

256

257

The CCD time-series analysis displays the changes in the AoI over time for the Kherba landslide. The dark region represents the main changes that occurred during the co-event period (earthquake date). The landslide shape is divided into two toes at the lower side of the Hill, as shown in Figs. 11 and 12. During the first week following the earthquake, changes are detected in the lower side of the hill and lasted until the late date of August 2020 (IFG-8 orbits 66, IFG-27 orbit 161, and IFG-20 for orbit 59). Afterwards, many other sources of noise were present in the AoI, which makes this technique less efficient (weather, human activities). Most of the processed images are 6 days' intervals, except the orbit 161 in which the co-event interferogram (IFG-24) was not good enough (bad coherence) to compare with other pre-post-event images, so it was replaced by the IFG-22. Figures 14 and 15 illustrate how the interferograms selection may change the interpretation of results.

258

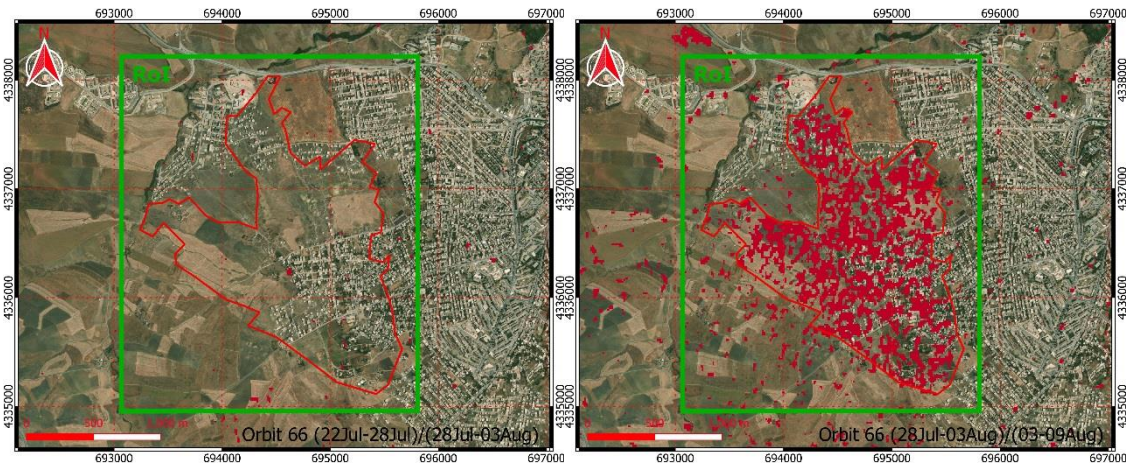
259

260

261

262

To quantify the change, an RoI represented in Fig. 13 (green rectangle) is selected for analysis. The plots in Figs. 14 and 15 show also the frequency distributions of coherence values within the RoI. Table 3 displays the calculated average coherence values of the RoI and the percentage of changes. For the orbit 66 pairs, the RoI average coherence starts by 0.66 during the pre-event period (IFG-2) and decreases to 0.51 during the co-event period (-23%) (IFG-3). For orbit 59 pairs, it decreases by 22% after an initial mean value of 0.77 (IFG-16) and a mean value of 0.60 (IFG-17).



263

264

265

Figure 13. Pre-event coherences ratio (left), co-event coherences ratio (right), Sentinel-1 Orbit 66. The green box indicates the scope of the RoI, red spots represent significant changes of coherence in the landslide region (QGIS, ESRI World Imagery basemap).

266

The last orbit 161 pairs make an exception due to the initial bad coherence maps (IFG-23 and 24), as shown in Fig. 15, where the dotted green line has low coherence compared to the co-event coherence map (red dotted line). So, the orbit 161 acquisition of the 3rd August must be skipped and not used for the analysis. It was replaced by the previous acquisition on July 28th. However, the previous pair (IFG-21 and IFG-22) had a value of 0.57 (IFG-21) that decreased to 0.52 (IFG-22), representing a 9 percent of change.

271

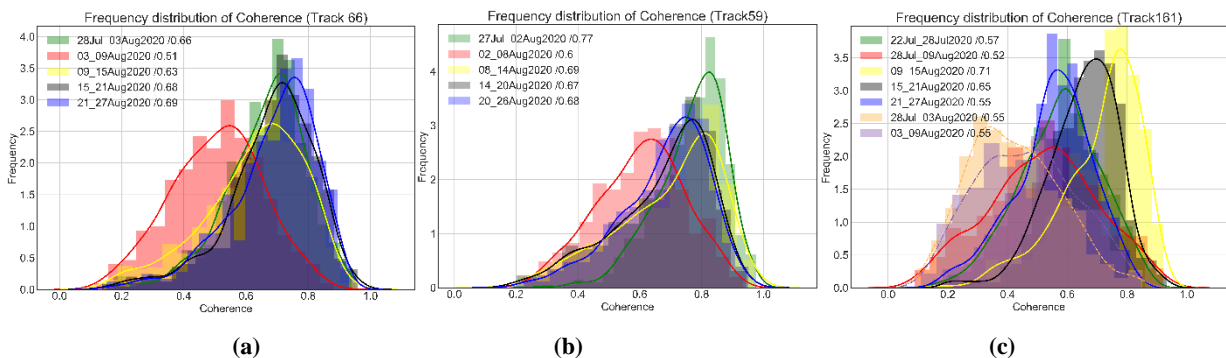
Table 3. Mean coherence change values inside the ROI.

Orbit	Pre-event coherence mean	Co-event coherence mean	Post-event coherence mean	Pre-event Change	Post-event Change
66	28Jul_03Aug	03_09Aug	09_15Aug	-23%	+24%
	0.66	0.51	0.63		
59	27Jul_02Aug	02_08Aug	08_14Aug	-22%	+15%
	0.77	0.60	0.69		
161	22Jul_28Jul	28Jul_09Aug	09Aug_15Aug	-9%	+37%
	0.57	0.52	0.71		

272

The lines in Figure 14 indicate the frequency distributions of coherence time series maps. The green line in Fig.14.a represents the pre-event coherence distribution, while the red line represents the post-event coherence distribution, which clearly shows a decay of the mean coherence after the main event (dates and values are presented in the legend).

274



275

276

277

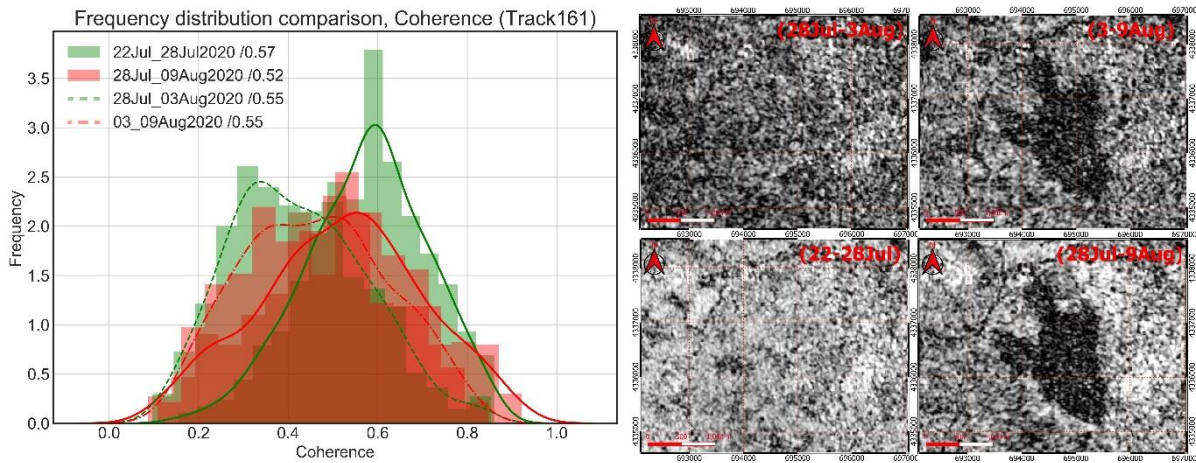
Figure 14. Frequency distributions of coherence values within RoI for all coherence time series images.

278

Figure 15 illustrates why the interferogram of the 22-28July (green line) is chosen as the pre-event (initial) even though there is another IFG of (28July-3Aug green dotted line) i.e. only four days before the main event (7 August 2020).

279

280



281

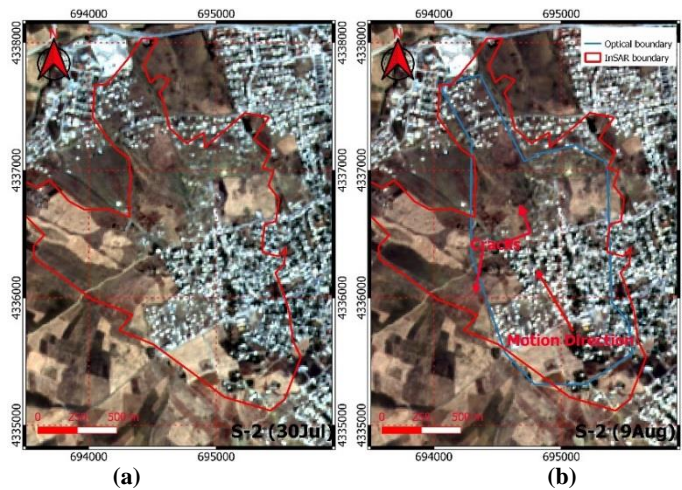
282 **Figure 15.** Effect of bad coherence: the cause is the acquisition of 3rd August start at (17:28:15, orbit 161) under bad weather conditions in
 283 the acquisition time according to precipitation site (WVO) (rainfall in that daytime), compared to the acquisition of the same day but not
 284 the same time (05:37:58 for orbit 66).

285 The surface area derived from the coherence images covers 2.1 km², and the shape ends by two toes. The runout distance
 286 is 2.4 km for the right toe and 2.15 km for the left one. The CCD method has the potential to differentiate between the areas
 287 impacted by induced changes and those affected by other sources of noise. The ratio operation is useful in canceling out other
 288 noise factors and improving the detection of changes in the region.

289 **4.2.2 Optical detection**

290 To validate the SAR methods results, two images from Sentinel-2 are downloaded and treated using QGIS software, the dates
 291 of the images are 2020-07-30 (a week before the main shock), and 2020-08-09 (two days after the main shock).

292 - The optical detection shows that an important displacement affected the ground in the Kherba neighborhood, over an area
 293 of 1.32 km². The landslide shape of deformation has only one toe at the lower part of the hill (blue line Fig. 16.b) compared
 294 to the CCD method results.



295

296

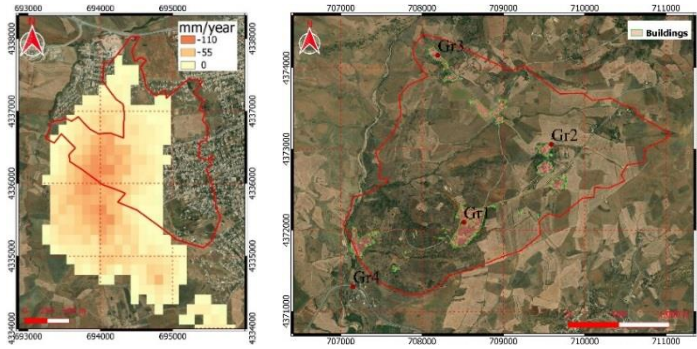
297

298 **Figure 16.** Sentinel-2 Optic Images: (a)- dated 30-Jul 2020, (b)- dated 09-Aug 2020.
 299 - The optical images were unable to detect the ground deformations and displacements in Grarem in which there was no
 300 apparent landslide although there were a lot of ruptures and cracks. However, a field inspection has confirmed the results
 of the CCD and DInSAR analysis in terms of pattern and limits of the zone affected by the deformation (surface rupture).

301 **4.3 LiCSBAS analyses**

302 Displacement time series and velocities analysis of the region is performed out using LiCSBAS that exploits the data of the
 303 LiCSAR system (Morishita, 2021). It allows identifying whether unstable conditions pre-existed or are still undergoing. The

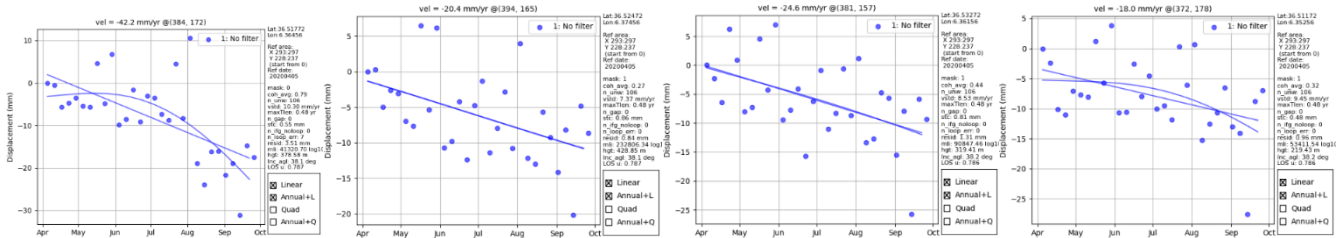
304 study started from the 5th of April to the 26th of September 2020, for the orbit 66 and from 26 April 2015 to 26 September 2020
 305 for the orbit N° 161.



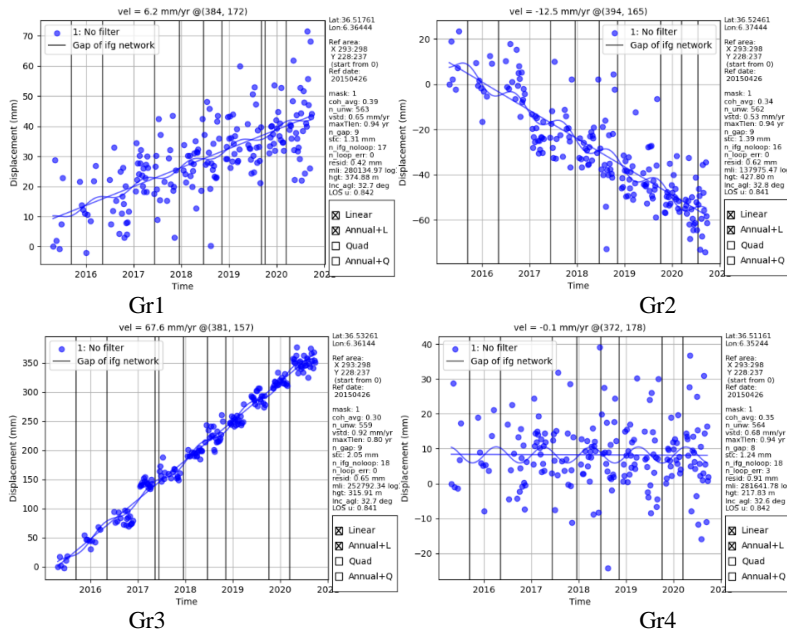
306
 307 **(a) (b) Figure 17.** (a) Line of sight displacement velocity map, the red line is landslide area (066D_05394_131311), (b)
 308 Grarem case selected points for time-series analysis, (QGIS, ESRI basemap).

309 The time-series analysis detected subsidence of the west part of Kherba. This region is on the other hillside of Kherba Hill,
 310 and both sides have a significant slope. A site investigation did not find any drilled wells. One may assume that this subsidence
 311 is not caused by the pumping of groundwater. Therefore, another possible explanation is probably related to the large mass
 312 movement of the main landslide hillside (red polygon), causing the opposite side of the hill to move down (subsidence). The
 313 displacement velocity in Kherba is about 110 mm/year, Fig. 17.

314 For the Grarem case, the velocity map looks stable between the same dates (April 5 to September 26, 2020). The change
 315 occurred rapidly and is removed by the filters. For illustrative purposes, the displacement time series of some points are
 316 illustrated in Figs. 18 and 19.



317
 318
 319 **Figure 18.** Displacement time series (orbit 66, Grarem case), corresponding to the points in image (17.b), the displacement is relative to a
 320 reference point, the plots present a great dispersion of data points which is related to many noise resources (weather, man-made, etc.), and
 321 short period of analysis, (QGIS, ESRI basemap).



322
 323
 324
 325
 326 **Figure 19.** Displacement time series (orbit 161), corresponding to the points in Fig. 17.b, The plots show less dispersion of data points
 327 (linear) compared to short analysis, the long period analysis (5 years) is useful to eliminate other sources of noise.

328 During the LiCSBAS processing, a primary stable reference point is selected at (36.455885° N, 6.276909° E). This method
329 proves to be efficient for large-scale deformation monitoring and slow coherent changes, long time series analysis is useful in
330 reducing other noise factors.

331 4.4 Discussion

332 InSAR monitoring proves its ability to detect land changes. First, landslides and land deformation can be detected remotely by
333 InSAR. Furthermore, optical images could detect only one case (Kherba). The theoretical results were validated by site visiting
334 and investigation, i.e.:

- 335 - Compared to results obtained from optical for the Kherba landslide, InSAR is more precise for detecting small
336 deformation (2 toes in CCD maps). Besides, the optical analysis did not detect the full deformed area in the region (only
337 one toe).
- 338 - Large-scale landslides exceed DInSAR's capabilities, which induce an extreme loss of coherence. The co-event
339 interferograms are strongly decorrelated. Therefore, the phase information is no longer usable and one cannot measure
340 the displacement of incoherent ground changes (Landslide).
- 341 - Land deformation in Grarem first detected by DInSAR, was confirmed by a site visit, during which small cracks were
342 visible on the ground (incoherent boundary region). Due to incoherent boundaries and because the displacement is
343 probably larger than what can be measured by one fringe cycle (depending on the wavelength, 5 cm for Sentinel-1), the
344 deformation measurements in this case are not reliable and accurate.
- 345 - Another landslide detected by InSAR in the Azeba region (6 km east of Mila) was visited too: the area covers 0.42 km²
346 and the site investigation confirms the landslide (Fig. 20).
- 347 - Analysis with LiCSBAS revealed new hillside deformation (subsidence) which is probably a consequence of the mass
348 that moved in the main landslide hillside. Displacements time series, of the Grarem region at some points, show
349 deformation along LOS with velocities ranging from 6 mm/year to 67 mm/year. This method is preferable in large-scale
350 area and long-period analysis.



351
352 **Figure 20.** Landslide occurred in Azeba region (2 km North) detected by InSAR: (a) & (b)- visible ground cracks, (c)- coherence map of
353 Azeba zone delimited by the cracks.
354

355 5 Conclusions and Recommendations

356 In this paper, active and passive space-based satellite data are used to monitor and study the impact of natural hazards
357 (earthquakes and landslides) on struck areas. The C-band Sentinel-1 SAR datasets (active sensing) and optical images of
358 Sentinel-2 data (10 m spatial resolution) were used in this study to investigate the area, the passive images were used only to
359 validate the active sensing results. For the InSAR processing, the use of DInSAR, CCD methods, and the LiCSBAS tools have
360 been able to generate a detailed time series analysis of ground changes.

361 InSAR techniques have proved their efficiency to extract useful geodetic information, such as the ground movement and track
362 surface deformation over large areas with centimetric accuracy in coherent change cases. The present research study has

363 demonstrated that the InSAR processing is adapted to study earthquake and landslides zones. As a result, three primary land
364 failures were detected over the study area using InSAR.
365 DInSAR is poorly suited to track and detect landslides. It is represented as a pixel decorrelation in phase interferograms and
366 high decay in coherence values. CCD is further suitable to map earthquake-induced landslides that may remain undetected
367 using coherent methods (DInSAR). The estimation of their horizontal/vertical displacements is a challenge to be inferred.
368 The Grarem deformation looks like a landslide that has just been initiated but might extend under an upcoming triggering
369 event. Actually, the failure plane rim is presented as a dark line in the coherence map or as the fringe circumference in phase
370 maps (estimated area 3.94 sq. km). This impending land failure needs therefore a thorough and real-time monitoring by the
371 PS-InSAR method, which can provide efficient and low-cost monitoring method able to obtain millimeter-level precision
372 displacement measurements over selected points in the area (Jia et al., 2019), and adequate geotechnical studies.
373 It is worth increasing awareness of possible future geotechnical threats in a timely manner, through on-site monitoring using
374 GPS, crack meters, and by placing inclinometers in the Grarem area, in order to develop a model of the slope stability.

375 **Acknowledgments:** In this work, we used SNAP and QGIS to analyze and plot maps. The authors are grateful to European
376 Space Agency (ESA) for providing freely the data through Copernicus Program and COMET.

377 **Conflicts of Interest:** The authors declare no conflict of interest.

378 **References**

- 379 ASF DAAC: Alaska Satellite Facility, [online] Available from: <https://search.asf.alaska.edu/#/> (Accessed 26 June 2021), n.d.
- 380 Bakon, M., Perissin, D., Lazecky, M. and Papco, J.: Infrastructure Non-linear Deformation Monitoring Via Satellite Radar
381 Interferometry, *Procedia Technol.*, 16, 294–300, doi:10.1016/j.protcy.2014.10.095, 2014.
- 382 Braun, A.: Radar satellite imagery for humanitarian response: Bridging the gap between technology and application, , 225
383 [online] Available from: https://publikationen.uni-tuebingen.de/xmlui/bitstream/handle/10900/91317/Braun_2019_Radar_satellite_imagery_for_humanitarian_response_UB.pdf?sequence=1, 2019.
- 385 Canaslan Çomut, F., Gürboğa, Ş. and Smail, T.: Estimation of co-seismic land deformation due to Mw 7.3 2017 earthquake
386 in Iran (12 November 2017) using Sentinel-1 DInSAR, *Bull. Miner. Res. Explor.*, 162(August), 11–30,
387 doi:10.19111/bulletinofmre.604026, 2020.
- 388 Cascini, L., Peduto, D., Pisciotta, G., Arena, L., Ferlisi, S. and Fornaro, G.: The combination of DInSAR and facility damage
389 data for the updating of slow-moving landslide inventory maps at medium scale, *Nat. Hazards Earth Syst. Sci.*, 13(6), 1527–
390 1549, doi:10.5194/nhess-13-1527-2013, 2013.
- 391 Congedo, L.: Semi-Automatic Classification Plugin: A Python tool for the download and processing of remote sensing
392 images in QGIS, *J. Open Source Softw.*, 6(64), 3172, doi:10.21105/joss.03172, 2021.
- 393 Del, M. and Idrogeologico, R.: Landslides forecasting analysis by displacement time series, *Geology*, 2011(January), 19–23,
394 2012.
- 395 ESA: ESA’s radar observatory mission for GMES operational services. [online] Available from:
396 https://sentinel.esa.int/documents/247904/349449/S1_SP-1322_1.pdf, 2012.
- 397 ESA: Resolution and Swath - Sentinel-1 - Missions - Sentinel Online - Sentinel, [online] Available from:
398 <https://sentinel.esa.int/web/sentinel/missions/sentinel-1/instrument-payload/resolution-swath> (Accessed 26 June 2021a), n.d.
- 399 ESA: SAR Instrument - Sentinel-1 SAR Technical Guide - Sentinel Online - Sentinel, [online] Available from:
400 <https://sentinels.copernicus.eu/web/sentinel/technical-guides/sentinel-1-sar/sar-instrument> (Accessed 26 June 2021b), n.d.
- 401 Frizon de Lamotte, D., de Lamotte, D. F., Bezar, B. Saint, Bracène, R. and Mercier, E.: The two main steps of the Atlas
402 building and geodynamics of the western Mediterranean, *Tectonics*, 19(4), 740–761 [online] Available from:

403 https://www.academia.edu/29649745/The_two_main_steps_of_the_Atlas_building_and_geodynamics_of_the_western_Mediterranean (Accessed 6 January 2022), 2000.

404

405 Galve, J. P., Castañeda, C. and Gutiérrez, F.: Railway deformation detected by DInSAR over active sinkholes in the Ebro

406 Valley evaporite karst, Spain, *Nat. Hazards Earth Syst. Sci.*, 15(11), 2439–2448, doi:10.5194/nhess-15-2439-2015, 2015.

407 Goudarzi, M. a: Detection and measurement of land deformations caused by seismic events using InSAR, Sub-pixel

408 correlation, and Inversion techniques, , (January), 127, 2010.

409 Herrera, G., Fernández, J. A., Tomás, R., Cooksley, G. and Mulas, J.: Advanced interpretation of subsidence in Murcia (SE

410 Spain) using A-DInSAR data - Modelling and validation, *Nat. Hazards Earth Syst. Sci.*, 9(3), 647–661, doi:10.5194/nhess-9-647-2009, 2009.

411

412 Hooper, A., Zebker, H., Segall, P. and Kampes, B.: A new method for measuring deformation on volcanoes and other natural

413 terrains using InSAR persistent scatterers, *Geophys. Res. Lett.*, 31(23), 1–5, doi:10.1029/2004GL021737, 2004.

414 Jacquemart, M. and Tiampo, K.: Leveraging time series analysis of radar coherence and normalized difference vegetation

415 index ratios to characterize pre-failure activity of the Mud Creek landslide, California, *Nat. Hazards Earth Syst. Sci.*, 21(2),

416 629–642, doi:10.5194/nhess-21-629-2021, 2021.

417 Jia, H., Zhang, H., Liu, L. and Liu, G.: Landslide deformation monitoring by adaptive distributed scatterer interferometric

418 synthetic aperture radar, *Remote Sens.*, 11(19), 1–18, doi:10.3390/rs11192273, 2019.

419 Jung, J. and Yun, S. H.: Evaluation of coherent and incoherent landslide detection methods based on synthetic aperture radar

420 for rapid response: A case study for the 2018 Hokkaido landslides, *Remote Sens.*, 12(2), 1–26, doi:10.3390/rs12020265,

421 2020.

422 Kim, J. W.: Applications of Synthetic Aperture Radar (SAR)/ SAR Interferometry (InSAR) for Monitoring of Wetland

423 Water Level and Land Subsidence, *Ohio State Univ.*, (503), 1–111, 2013.

424 Laneve, G., Bruno, M., Mukherjee, A., Messineo, V., Giuseppetti, R., De Pace, R., Magurano, F. and Ugo, E. D. ': Remote

425 Sensing Detection of Algal Blooms in a Lake Impacted by Petroleum Hydrocarbons, *Remote Sens.* 2022, Vol. 14, Page 121,

426 14(1), 121, doi:10.3390/RS14010121, 2021.

427 Lazecký, M., Hatton, E., González, P. J., Hlaváčová, I., Jiráňková, E., Dvořák, F., Šustr, Z. and Martinovič, J.:

428 Displacements monitoring over Czechia by IT4S1 system for automatised interferometric measurements using Sentinel-1

429 data, *Remote Sens.*, 12(18), 1–21, doi:10.3390/RS12182960, 2020a.

430 Lazecký, M., Spaans, K., González, P. J., Maghsoudi, Y., Morishita, Y., Albino, F., Elliott, J., Greenall, N., Hatton, E.,

431 Hooper, A., Juncu, D., McDougall, A., Walters, R. J., Watson, C. S., Weiss, J. R. and Wright, T. J.: LiCSAR: An automatic

432 InSAR tool for measuring and monitoring tectonic and volcanic activity, *Remote Sens.*, 12(15), doi:10.3390/RS12152430,

433 2020b.

434 LNHC: Laboratoire National de l'Habitat et de la Construction, LNHC [online] Available from: <http://lnhc-dz.com/>

435 (Accessed 26 June 2021), n.d.

436 Meng, Q., Confuorto, P., Peng, Y., Raspini, F., Bianchini, S., Han, S., Liu, H. and Casagli, N.: Regional recognition and

437 classification of active loess landslides using two-dimensional deformation derived from sentinel-1 interferometric radar

438 data, *Remote Sens.*, 12(10), doi:10.3390/rs12101541, 2020.

439 Merghadi, A., Abderrahmane, B. and Tien Bui, D.: Landslide susceptibility assessment at Mila basin (Algeria): A

440 comparative assessment of prediction capability of advanced machine learning methods, *ISPRS Int. J. Geo-Information*,

441 7(7), doi:10.3390/ijgi7070268, 2018.

442 Moretto, S., Bozzano, F. and Mazzanti, P.: The role of satellite insar for landslide forecasting: Limitations and openings,

443 *Remote Sens.*, 13(18), 1–31, doi:10.3390/rs13183735, 2021.

444 Morishita, Y.: Nationwide urban ground deformation monitoring in Japan using Sentinel-1 LiCSAR products and LiCSBAS,

445 *Prog. Earth Planet. Sci.*, 8(1), doi:10.1186/s40645-020-00402-7, 2021.

446 Mouloud, H. and Badreddine, S.: Probabilistic seismic hazard assessment in the Constantine region, Northeast of Algeria,
447 Arab. J. Geosci., 10(6), doi:10.1007/s12517-017-2876-5, 2017.

448 Netzband, M., Stefanov, W. L. and Redman, C.: Applied remote sensing for urban planning, governance and sustainability.,
449 2007.

450 Pawluszek-Filipiak, K. and Borkowski, A.: Integration of DInSAR and SBAS techniques to determine mining-related
451 deformations using Sentinel-1 data: The case study of rydultowy mine in Poland, Remote Sens., 12(2),
452 doi:10.3390/rs12020242, 2020.

453 Peláez Montilla, J. A., Hamdache, M. and Casado, C. L.: Seismic hazard in Northern Algeria using spatially smoothed
454 seismicity. Results for peak ground acceleration, Tectonophysics, 372(1–2), 105–119, doi:10.1016/S0040-1951(03)00234-8,
455 2003.

456 Rapant, P., Struhár, J. and Lazecký, M.: Radar interferometry as a comprehensive tool for monitoring the fault activity in the
457 vicinity of underground gas storage facilities, Remote Sens., 12(2), doi:10.3390/rs12020271, 2020.

458 Roque, D., Perissin, D., Falcão, A. P., Fonseca, A. M. and Maria, J.: Dams regional safety warning using time-series insar
459 techniques, Second Internatinal Dam World Conf., 21–24, 2015.

460 Sanabria, M. P., Guardiola-Albert, C., Tomás, R., Herrera, G., Prieto, A., Sánchez, H. and Tessitore, S.: Subsidence activity
461 maps derived from DInSAR data: Orihuela case study, Nat. Hazards Earth Syst. Sci., 14(5), 1341–1360, doi:10.5194/nhess-
462 14-1341-2014, 2014.

463 Tampuu, T., Praks, J., Uiboupin, R. and Kull, A.: Long term interferometric temporal coherence and DInSAR phase in
464 Northern Peatlands, Remote Sens., 12(10), 7–9, doi:10.3390/rs12101566, 2020.

465 Tzouvaras, M., Danezis, C. and Hadjimitsis, D. G.: Small scale landslide detection using Sentinel-1 interferometric SAR
466 coherence, Remote Sens., 12(10), doi:10.3390/rs12101560, 2020.

467 USGS: M 5.0 - 3 km NNE of Sidi Mérouane, Algeria, [online] Available from:
468 <https://earthquake.usgs.gov/earthquakes/eventpage/us6000bag6/executive> (Accessed 26 June 2021a), n.d.

469 USGS: USGS Earthquake Hazards Program, [online] Available from: <https://earthquake.usgs.gov/> (Accessed 26 June
470 2021b), n.d.

471 Wang, Z., Li, Z. and Mills, J.: A new approach to selecting coherent pixels for ground-based SAR deformation monitoring,
472 ISPRS J. Photogramm. Remote Sens., 144, 412–422, doi:10.1016/j.isprsjprs.2018.08.008, 2018.

473 Wempen, J. M.: International Journal of Mining Science and Technology Application of DInSAR for short period
474 monitoring of initial subsidence due to longwall mining in the mountain west United States, Int. J. Min. Sci. Technol., 30(1),
475 33–37, doi:10.1016/j.ijmst.2019.12.011, 2020.

476 WWO: Mila, Mila, Algeria Historical Weather Almanac, [online] Available from:
477 <https://www.worldweatheronline.com/mila-weather-history/mila/dz.aspx> / (Accessed 26 June 2021), n.d.

478